Verification of Spherical Mathematical Absorber Reflection Suppression in a Combination Spherical Near-Field and Compact Antenna Test Range

S.F. Gregson[1,2] , A.C. Newell[1], P.N. Betjes[1]
[1]NSI-MI Technologies LLC.,
19730 Magellan Drive,
Torrance,
CA 90502-1104, USA

C.G. Parini[2]
[2]Queen Mary University of London
School of Electronic Engineering and Computer Sciences
Peter Landin Building,
10 Godward Square
London UK E1 4FZ

Abstract—**This paper presents the results of a recent study concerning the computational electromagnetic simulation of a spherical near-field (SNF) antenna test system in the presence of a compact antenna test range (CATR). The plane-wave scattering matrix approach [1, 2] allows many of the commonly encountered components within the range uncertainty budget, including range reflections, to be included within the model [3]. This paper presents the results of simulations that verify the utility of the spherical mathematical absorber reflection suppression (S-MARS) technique [3, 4] for the identification and subsequent extraction of artifacts resulting from range reflections. Although past verifications have been obtained using experimental techniques this paper, for the first time, corroborates these findings using purely computational methods. The use of MARS is particularly relevant in applications that inherently include scatterers within the test environment. Such cases include instances where a SNF test system is installed within an existing compact antenna test range (CATR) as is the configuration at the recently upgraded Queen Mary University of London (QMUL) Antenna Laboratory [5, 6]. Thus, this study focuses on this installation with results of CEM simulations being presented. The method enables a quantitative measure of the levels of suppression offered by the MARS system.**

I. INTRODUCTION

As is the case with other forms of near-field testing, in many instances, spherical scanning can have the integrity of the antenna measurement compromised by: range reflections (*i.e.* clutter), truncation and contamination by random noise with these terms often being found to constitute some of the larger components within the range uncertainty budget [3]. The measurement and post-processing mode orthogonalisation and filtering technique, called Mathematical Absorber Reflection Suppression (MARS) [3, 4] has been extensively employed to identify and then extract measurement artefacts arising from spurious scattering that are present when antenna testing is conducted within imperfect anechoic environments. Thus, spherical MARS is routinely deployed when spherical near-field testing. Underpinning the success of all forms of the MARS post-processing is the behavior of the orthogonal vector wave (mode) expansions under isometric co-ordinate system translations [3, 7]. Computational electromagnetic simulations have been utilized to illustrate this behavior and to further

verify the effectiveness of MARS processing [3, 7]. However, this sort of detailed examination has been relatively limited in scope. Thus, in order that the behavior of the SMCs under S-MARS processing could be examined and illustrated in the absence of other spurious measurement errors, the use of a computational electromagnetic (CEM) simulation was utilized. A numerical approach was preferable, as analytical verification techniques are generally complicated by the difficulty with which closed form analytical solutions are obtained, and even when exact solutions do exist, they tend to be awkward and difficult to use. This is especially true for complex configurations such as those inherent to the S-MARS technique.

II. SIMULATION METHODOLOGY

Any near-field measurement can be simulated by determining the complex coupling coefficient between the guided-wave port on the AUT and the guided-wave port near-field probe at each position across the intended acquisition surface for each of the two orthogonal tangential polarizations at each frequency. In principle, it would be possible to obtain these transmission coefficients from a full-wave three-dimensional electromagnetic (EM) solver and this approach would have the advantage of introducing the smallest number of approximations and assumptions providing, in principle, the most accurate measurement simulation possible. However, although many such solvers are available, they are typically thought to be inappropriate for simulating problems such as that being considered here where each measurement point corresponds to a completely independent, separate simulation and each individual simulation itself comprises an electrically large problem-space. This limitation is a result of the very long processing times and the (often) not inconsiderable amounts of computer resources required. Hence, moving to less general, but more efficient approach becomes very attractive [3, 7]. In this case, the plane-wave spectrum (PWS) method [3] was harnessed to reconstruct the radiated near electric field across a spherical surface from the far-field antenna pattern. Additionally, it is also possible to use a planar aperture illumination function to initialize the simulation requiring an additional step of first performing a near-field to far-field transform to obtain the necessary far-field pattern, or plane

wave spectrum (PWS). This PWS based method is a general purpose technique that underpins standard planar near-field theory and is the basis of microwave-holographic-metrology [3]. The other great advantage of going via the far-field, or PWS, is that it greatly simplifies the task of including additional stutterers or sources which is an important consideration in this work. The radiated near-field can be reconstructed across the surface of a hemisphere where z > 0 using [3],

$$
\underline{E}(x,y,z) = \frac{1}{\lambda^2} \int_{-\infty}^{\infty}\int_{-\infty}^{\infty}\left[\left(\underline{\hat{u}}_x - \underline{\hat{u}}_z \frac{u}{w}\right)F_x(u,v)\right.
$$
$$
\left. + \left(\underline{\hat{u}}_y - \underline{\hat{u}}_z \frac{v}{w}\right)F_y(u,v)\right]e^{-jk_0(ux+vy+wz)}dudv \quad (1)
$$

Here, F_x and F_y are respectively, the x- and y-polarised angular spectra, the conventional Cartesian and spherical coordinates are related by $x = r\sin\theta\cos\phi$, $y = r\sin\theta\sin\phi$ and $z = r\cos\theta$ where $0 \le \theta \le 2\pi$, $0 \le \phi \le 2\pi$, and $r \ge 0$ [3]. This is illustrated in Figure 1 below. The reconstructed Cartesian near electric field components are sampled using a monotonic plaid and equally spaced θ, ϕ grid. The near electric field can be resolved onto a conventional spherical polarization basis [3] whereupon the resulting near-field data is in a form that is immediately suitable for processing with a standard spherical near-field to far-field transformation [3].

A result of the application of equation (1) and the projection of the fields onto a spherical polarisation basis is illustrated in Figure 2. Figure 2 contains therefore a false-colour plot over a conceptual spherical measurement surface of the θ-polarized component of the near electric field of a uniformly illuminated square aperture of side 0.356 m cut in an infinitely thin perfect electric conducting (PEC) ground-plane of infinite extent that is coincident and synonymous with the *xy*-plane. This plane was offset from the origin of the spherical measurement coordinate system by 0.51 m (20 inches) in the z-direction to form a conventional MARS type measurement [3, 4].
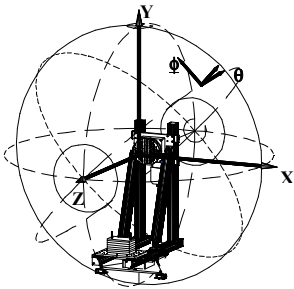

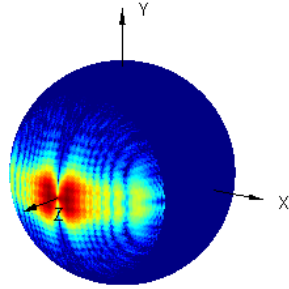Figure 1. φ/θ coordinate system with polar axis = z-axis, source polarization fixed during then measurement.

Figure 2. Simulated θ-polarised near electric field component plotted over the spherical surface, 50 dB amplitude colour scale.

III. SIMULATED SPHERICAL NEAR-FIELD MARS MEASUREMENTS & S-MARS VERIFICATION

The standard spherical transmission formula permits the AUT and the probe to be described by spherical mode coefficients that are the complex coefficients of basis functions that are elementary solutions of Maxwell's equations for a spherical coordinate system [3]. In principle, the spherical transmission equation is valid for any arbitrary test antenna and certain probe combinations at any separation distance between the spherical co-ordinate system origin and the probe that is outside of the minimum sphere of radius ρ_0 that will completely enclose the majority of the current sources. In a linear isotropic and homogeneous source or sink free space which is enclosed by a spherical surface and which is located at the origin of an inertial frame of reference, the electric field can be expressed as [3],

$$
\underline{E}(r,\theta,\phi) = k_0\sqrt{Z}\sum_{n=1}^{\infty}\sum_{m=-n}^{n}\left[Q_{TEmn}^{(3)}\underline{F}_{TEmn}^{(3)}(r,\theta,\phi)\right.
$$
$$
\left. + Q_{TMmn}^{(3)}\underline{F}_{TMmn}^{(3)}(r,\theta,\phi)\right] \quad (2)
$$

Here, $Q_{TMmn}^{(3)}$ and $Q_{TEmn}^{(3)}$ denote the transverse magnetic (TM) and transverse electric (TE) spherical mode coefficients, which are complex values of n and m, $\underline{F}_{TMmn}^{(3)}$ and $\underline{F}_{TEmn}^{(3)}$ are TM and TE spherical vector wave-functions which are functions of n, m, r, θ, ϕ. Here, spherical Hankel functions are used to represent radial outgoing waves [3]. The spherical mode coefficients (SMC) are complex numbers that are functions of frequency, the polarization index, the polar index n, and the azimuthal index m such that $0 \le n \le \infty$ and $-n \le m \le n$ which do not vary with any of the scanning coordinates. The summation can in practice not be infinite and instead the maximum value for the polar summation is truncated to a finite integer number, which is large enough to enable the field to be precisely and accurately and represented. This is discussed in greater detail below and in [3, 7].

Conversely, by using mode orthogonality, equation (2) can be inverted whereby the two orthogonal tangential near electric field components (one of which is shown in Figure 2 above) can be used to obtain the TM and TE SMCs using standard spherical processing [3]. The resulting TE SMCs are presented in Figure 3 below. As the study of the behavior of these coefficients under certain isometric transformations [3, 7] is the central theme of this paper, Figure 3 contains a false-color checkerboard plot of the magnitude of the SMCs prior to the application of a translation of origins. That is to say, Figure 3 presents the intensity of the SMCs corresponding to the case where the AUT has been offset from the origin of the measurement coordinate system during the simulated acquisition. Conversely, Figure 4 presents an equivalent set of SMCs to those shown in Figure 3, *i.e.* for the same AUT, only here the AUT has been mathematically translated back to the origin of the spherical measurement coordinate system [3, 7]. Prior to the translation, the AUT had been displaced away from the origin of the measurement coordinate system in the z-axis direction, *cf.* Figures 1 and 2, by 0.51 m (20"). The displacement of the AUT from the measurement origin produces a far more complex phase variation within the measured spherical near fields. The greater the complexity of

the phase function, the greater the need for power within higher order SMCs and thus the broader the distribution of the associated spherical mode spectrum [7]. In Figure 4, the vertical black line denotes the highest order SMCs required by the standard spherical sampling theorem to represent a radiator of a given electrical size [3, 7]. This mode cut-off is determined by evaluating $n = \text{ceil}(k_0 r_{t0}) + n_s. = 55 + n_s$ where n is the highest order polar mode index associated with the AUT. Here, r_{t0} denotes the maximum radial extent (MRE) [3], k_0 is the free space propagation number, n_s is a positive integer that is used as a safety margin that depends upon the accuracy required and ceil is a function that rounds towards positive infinity. The MRE is the radius of a conceptual sphere that is centered about the origin of the measurement coordinate system that is large enough to circumscribe the majority of the current sources in the AUT.
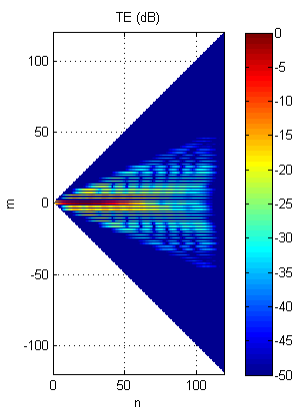
Figure 3. Amplitude plot of SMCs for an AUT when its aperture is displaced from the measurement origin.
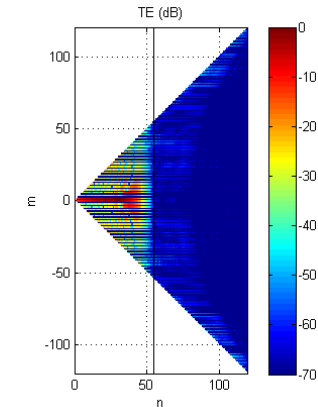
Figure 4. Amplitude plot of SMCs for an AUT when its aperture is at the measurement origin.

In order that the new model could be verified, the simulated spherical near-field data was transformed from the near-field to the far-field using a standard spherical mode expansion [3] with the input and output probes being specified as being infinitesimal electric dipoles [3, 7]. The resulting far-field patterns were compared with the initial far-field antenna pattern, *i.e.* the reference, with the azimuth and elevation great circle cuts being presented respectively in Figures 5 and 6 below. Here, the red traces denote the reference patterns, the blue trace is the transformed far-field data and the black trace is the spherical MARS processed pattern. It is clear that the results are in very good agreement with only minor differences being observed between the transformed and reference patterns at large pattern angles in the azimuth plane where effects associated with spherical mode leakage and near-field truncation are observed. This is expected as the spherical near-field simulation only provided pattern data over a half space meaning that an infinitely large number of SMCs would be required to represent the field discontinuity encountered by the tangential electric field when it is shorted out at the intersection with the conducting ground plane. However this is a sufficiently small, localized, effect that is can be ignored for the purposes being considered here.
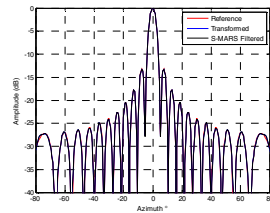

Figure 5. Comparison of reference far-field azimuth cut and transformed near-field data with and without MARS.
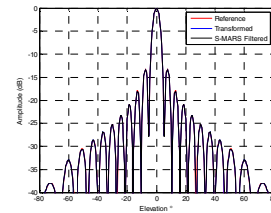
Figure 6. Comparison of reference far-field elevation cut and transformed near-field data with and without MARS.

IV. PRELIMINARY S-MARS RESULTS

As the spherical near-field "measurement" model is shown to be reliable, an initial test was conducted to confirm that the behavior of the SMCs in the model is consistent with what is encountered experimentally. As such, a spurious radiator was incorporated into the measurement simulation. This perturbed spherical near-field data set was transformed, using standard spherical processing, and the resulting SMCs can be seen presented in Figure 7 below for the case where the AUT has been mathematically translated (by 0.51 m) back to the origin of the measurement coordinate system. Here, the SMCs associated with the AUT can be seen towards the "tip" of the spectrum pattern in the vicinity of lower order m and n mode indices. Conversely, the modes associated with the scatterer, seen towards the right of the plot, have been displaced towards higher order modes, *cf.* especially in the region where $n > 100$.
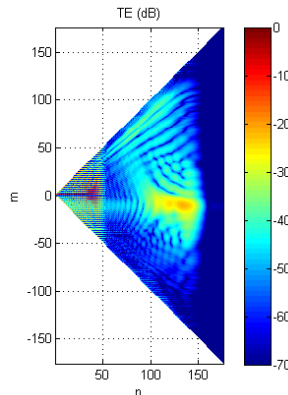

Figure 7. Amplitude plot of SMCs showing mode orthogonalisation after AUT translated to origin.
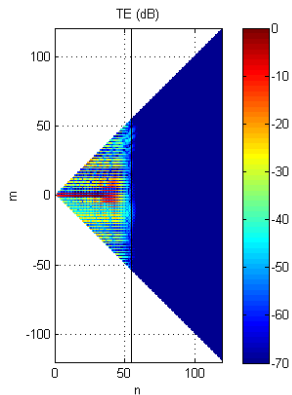
Figure 8. Amplitude plot of SMCs with S-MARS filtering applied, note the reduced scale of the axes.

These higher order modes can be filtered out as they correspond to modes that, as a consequence of the spherical sampling theorem, cannot be associated with the AUT. In this case, using the sampling theorem set out above, this corresponds to a polar mode index of *circa* 55. This is represented in Figure 8 with the vertical black line. Once filtered using a low pass mode filter function such that,

$$Q_{TEmn}^{(3)}\big|_{\text{Filtered}} = Q_{TEmn}^{(3)} f_m f_n \qquad (3)$$

$$Q_{TMmn}^{(3)}\big|_{Filtered} = Q_{TMmn}^{(3)} f_m f_n \qquad (4)$$

Where,

$$f_m = \begin{cases} 0.5^{(|m|-m_{Max})} & \text{when } |m| > m_{Max} \\ 1 & \text{elsewhere} \end{cases} \qquad (5)$$

$$f_n = \begin{cases} 0.5^{(n-n_{Max})} & \text{when } n > n_{Max} \\ 1 & \text{elsewhere} \end{cases} \qquad (6)$$

Here, m_{Max} and n_{Max} denote the highest order azimuthal and polar modes as determined by the spherical sampling theorem. This filtering corresponds to a linear attenuation when expressed in dB form. The resulting filtered mode function, *i.e.* Figure 8, is found to be in good agreement with the reference result, presented in Figure 4 above. Here, this mode filter was applied and the higher order modes were attenuated. Crucially, as the mode filter only acts upon higher order modes, the integrity of the underlying antenna pattern function is preserved irrespective of the complexity of that pattern making S-MARS processing equally effective with high and low gain antennas. Figure 9 shows a plot of the amplitude of the power contained within the n mode index for $m = 1$ which corresponds to taking a "horizontal" cut that passes through the center of the plot shown in Figure 7 above. Here, the blue trace represents a cut through the mode space prior to the AUT be translated back to the origin of the measurement coordinate system. The red trace represents the same data only here the AUT has been mathematically translated back to the origin of the measurement coordinate system prior to the SMCs being computed. The vertical magenta line denotes the $n = 55$ mode and lastly, the black trace represents the SMCs once the MARS filter has been applied. By way of a comparison, Figure 10 shows the SMCs for the case where the AUT has been translated back to the origin of the measurement coordinate system but where the simulated measurement has *not* been perturbed by the introduction of the spurious scatterer. As expected, it is evident from inspection of Figure 10 that the low order modes, *i.e.* those modes associated with the AUT (*i.e.* where $n < 55$) are in very close agreement, however the higher order modes, *i.e.* those modes which are predominately associated with the scatterer, diverge significantly.
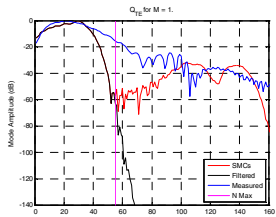

Figure 9.   Plot illustrating the effect of S-MARS processing on the SMCs.
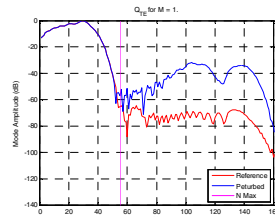

Figure 10.   Comparison of SMCs with and without being peturbed by spurious scattering.

Figure 11 shows the resulting far-field pattern that is obtained from using standard spherical near-field to far-field transformation to process the scatterer contaminated spherical near-field data. The effect of the spurious scatterer is evident in the pattern.
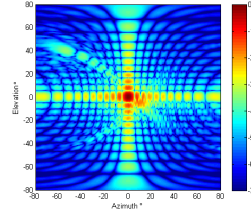

Figure 11.   Far-field pattern with scatterer included using standard spherical processing.
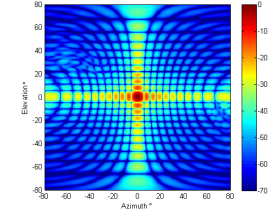

Figure 12.   Equivalent far-field pattern obtained using S-MARS processing.

Conversely, Figure 12 presents the result of applying S-MARS processing to the same data set that was used to create Figure 11. Here, it is clear that the spurious scatter has been very effectively extracted from the processed far-field data. A further comparison is shown in Figure 13 where an azimuth great circle cut is presented. Here, the reference pattern is denoted by the red trace, the perturbed pattern is shown in blue and the S-MARS processed pattern is shown in black. Thus, from inspection of Figure 13, it is clear that S-MARS has brought the reference and S-MARS processed results into very good agreement with one another. This simulation was repeated only this time, the scatterer was re-orientated so that the peak of the spectral reflection fell within the elevation pattern cut. Figure 14 shown the equivalent result where again is it clear that the S-MARS processing is very effectively suppressing the spurious signal.
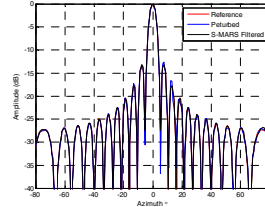

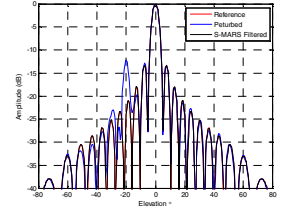Figure 13.   Azimuth cut comparing reference, peturbed and S-MARS processed pattern cut.

Figure 14.   Elevation cut comparing reference, peturbed and S-MARS processed pattern cut.

V.   PRELIMINARY S-MARS RESULTS IN THE PRESENCE OF A CATR

The previous section illustrated the effect that S-MARS processing has on suppressing artefacts associated with spurious scattering. In this section an equivalent simulation technique is harnessed to perturb the spherical near-field measurement with fields scattered by the sector shaped reflector that is present in the Queen Mary University of London (QMUL) antenna laboratory. Here, the 700S-60 based spherical near-field antenna test system is installed within an existing compact antenna test range so that commonality of positioners, chamber, heating ventilation & air conditioning (HVAC) and RF sub-system can be harnessed. The spherical near-field range can be used at frequencies that are conventionally thought of as being too low for the CATR to produce a high quality pseudo plane wave and conversely, the CATR can be used at higher frequencies and in cases where the

CATR is a more efficient instrument. The QMUL CATR can be seen presented in Figure 15 below. Here, the sector shaped parabolic reflector can be seen in the center of the picture. Towards the right hand side of the image, an absorber screen can be seen in its stowed position. Conversely, Figure 16 shows the absorber curtain fully deployed, as is the case when using the sub-mm-wave tri-reflector CATR, which can also be seen here. The absorber curtain offers a good degree of attenuation however; its reflectivity is less than that which is provided by the taller pyramidal absorber that is used to cover the interior of the CATR chamber. Further details of the QMUL CATR can be found in the open literature [3, 5].

The purpose of this modelling campaign was twofold. Firstly, to establish the nature of the scattering that could be expected to be encountered when using the spherical near-field test system in the presence of the CATR reflector and secondly to examine how effective standard S-MARS processing would be for mitigating those effects.
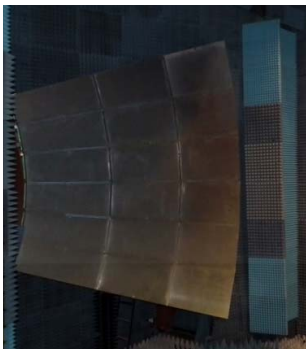

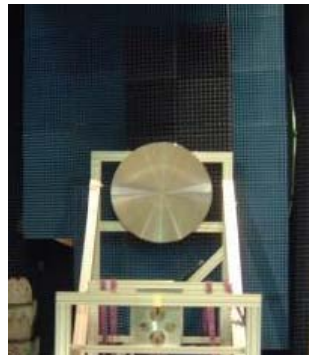Figure 15. Absorber curtain shown stowed when using large mm-wave CATR.

Figure 16. Absorber curtain shown deployed when using sub-mm-wave tri-reflector CATR.

The pseudo plane wave that is produced by the feed and reflector combination has been studied extensively with details of the simulation being presented in [8, 9, 10]. This physical optics, current element, based simulation tool was used to compute the electric field across a plane that is transverse to the boresight direction of the range. A false color plot of the amplitude of the horizontally polarized electric field component can be found presented in Figure 17 below. The equivalent angular spectrum of plane waves was computed using (8) with the amplitude of the spectrum being presented in Figure 18.

$$\underline{F_T}(u,v) = \int\limits_{-\infty}^{\infty}\int\limits_{-\infty}^{\infty} \underline{E_T}(x,y,z=0) e^{jk_0(ux+vy)} dx\, dy \qquad (7)$$

Here, $\underline{E_T}$ denotes the tangential components of the electric field which are assumed to be acquired across a planar surface. A pure plane wave propagating the direction of the z-axis produced by an infinitely large aperture set in the xy-plane would correspond to a single plane wave component propagating in the direction $u = v = 0$ ($w = 1$). However, as the projected aperture of the CATR parabolic reflector is of finite size, i.e. 3 m in width the resulting spectrum will be more widely distributed than that of the perfect plane wave. The

trails of side-lobes that can be seen in Figure 18 result from diffraction from the reflector's sharply discontinuous knife-edge. The dispersed side-lobe trains emanate from diffraction from the curved section whereas the more closely grouped side-lobe trails correspond to the top and bottom straight edges. Note that the 8 GHz case being considered here is below the usual operating frequency of the mm-wave CATR which explains the higher than expected edge diffraction as reflector under illumination is not being used to manage the edge diffraction. However, this frequency is well within the frequency range that the spherical near-field system could reasonably be expected to be used and hence its adoption here.

Some 2nd order truncation effects are present within the computed PWS as the near-field of the pseudo plane wave was only circa 30 dB down at the edge of the simulation interval [3]. However, for the configuration being considered here, such low level spectral leakage is not significant and can be safely ignored. As in practice the AUT is typically placed at a position of $z = 1.33f$ where f corresponds to the 5.4 m focal length of the CATR, the plane wave spectrum can be expected to be truncated to include only propagating, homogeneous, plane-wave components as evanescent fields will have been attenuated beyond a few wavelengths meaning the limits of integration used in (1) to compute the equivalent spherical near-fields can be collapsed to $u^2 + v^2 \leq 1$ without loss of generality.
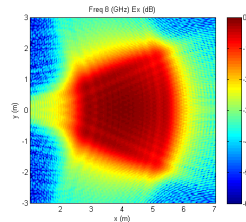

Figure 17. CATR pseudo plane-wave amplitude pattern plotted at 8 GHz.
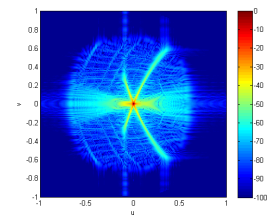
Figure 18. Plane-wave spectrum representation of CATR pseudo-wave.

For the purposes of this simulation the peak of the pseudo plane wave was assumed to be circa 12.5 dB below the peak of the AUT which corresponded to the S_{11} match of the corrugated horn that is used to feed the reflector. As an example, the fields were rotated by 17.5° in azimuth, although other angles were also tried, to represent the relative alignment between the boresight direction of the spherical near-field and compact antenna test ranges, cf. Figure 21 below. The resulting far-fields can be seen presented in Figure 19 below. Here, the peak of the CATR pseudo plane wave can be seen as a fine spot at azimuth =-17.5°, elevation = 0°. Although the polarization axis (i.e. χ-axis cf. Figure 1) of the CATR and the SNF ranges are at different heights within the chamber, the z-axis of the CATR is horizontal and thus the direction of the specular reflection would lie within the azimuth plane of far-field patterns obtained using the spherical system. As the CATR pseudo plane wave is 3m across, which corresponds to 80 wavelengths at 8 GHz, this corresponds to a very sharp pattern function with the diffraction-lobes falling very rapidly away from this direction.
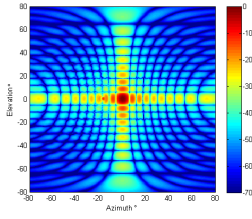
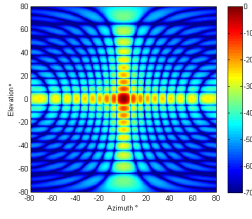Figure 19. Without FF-MARS showing CATR pseudo plane wave spot.

Figure 20. Far-field pattern with S-MARS processing applied.

Figure 20 shows the result of using S-MARS processing to attenuate the scattered fields. Figure 22 below shows a comparison of the far-field great circle cuts. Here, the unperturbed, *i.e.* reference, pattern cut is denoted by the red trace, the blue trace corresponds to the pattern when perturbed by the CATR pseudo plane wave, and the black trace represents the S-MARS processed pattern. From inspection of Figure 22 it is clear that the effects of the CATR reflector have been largely mitigated with the peak of the spike being reduced by more than 15 dB. However, some small residual does remain after processing and is present in the form of a small change in side-lobe level of the adjacent side-lobe.
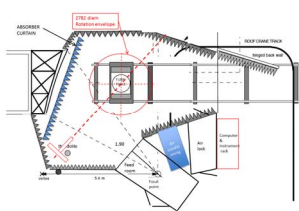

Figure 21. Plan-view schematic of QMUL combination CATR/SNF antenna test system.
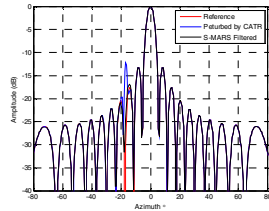

Figure 22. Far-field azimuth cut of AUT pattern with and without FF-MARS processing.

VI. SUMMARY AND CONCLUSIONS

In this paper the results of a new spherical near-field measurement simulation have been presented that have, for the first time, allowed the general effectiveness of spherical MARS processing to be verified using purely computationally means. This model has been used to simulate a conventional S-MARS measurement and to carefully verify the effectiveness of the S-

MARS technique and specifically to verify the use of S-MARS to manage the scattering from a CATR reflector in a combination SNF/CATR antenna test system. As this is a part of an ongoing study the future work is to include a measurement campaign to provide further experimental verification of the simulation results presented herein and to examine the effects of S-MARS processing on CATR QZ amplitude and phase ripple.

REFERENCES

[1] A.C. Newell, S.F. Gregson, "Estimating the Effect of Higher Order Modes in Spherical Near-Field Probe Correction", Antenna Measurement Techniques Association (AMTA) 34th Annual Meeting & Symposium, Bellevue, Washington October, 2012.

[2] A.C. Newell, S.F. Gregson, "Computational Electromagnetic Modelling Of Spherical Near-Field Antenna Test Systems Using Plane Wave Spectrum Scatting Matrix Approach", Antenna Measurement Techniques Association (AMTA) 36th Annual Meeting & Symposium, Tucson, Arizona, October, 2014.

[3] C.G. Parini, S.F. Gregson, J. McCormick, D. Janse van Rensburg "Theory and Practice of Modern Antenna Range Measurements", IET Press, 2014, ISBN 978-1-84919-560-7.

[4] G.E. Hindman, A.C. Newell, "Reflection Suppression in a large spherical near-field range", Antenna Measurement Techniques Association (AMTA) 27th Annual Meeting & Symposium, Newport, RI, October. 2005.

[5] A.D. Olver, C.G. Parini, "Millimetre-wave Compact Antenna Test Range", JINA Nice, November 1992.

[6] C.G. Parini, R. Dubrovka, S.F. Gregson, "CATR Quiet Zone Modelling and the Prediction of 'Measured' Radiation Pattern Errors: Comparison using a Variety of Electromagnetic Simulation Methods" Antenna Measurement Techniques Association (AMTA) 37th Annual Meeting & Symposium, Long Beach California, October 2015.

[7] S.F. Gregson, A.C. Newell, G.E. Hindman, "Behaviour of Orthogonal Wave Functions And The Correction of Antenna Measurements Taken in Non-Anechoic Environments", Loughbourugh Antenna Propagation Conference LAPC, Loughbourough, November, 2013.

[8] C.G. Parini, R. Dubrovka, S.F. Gregson, "Optimizing a CATR Quiet Zone using an Array Feed", Antenna Measurement Techniques Association (AMTA) 38th Annual Meeting & Symposium, Austin Texas, October 2016.

[9] S.F. Gregson, A.C. Newell, C.G. Parini, "Verification of Feed Spillover Reduction using

[10] FF-MARS in a CATR Using Computational Electromagnetic Simulation", IEEE Antennas and Propagation Society (APS), San Diego, July, 2017.